

Dendritic compartmentalization of input-specific integration and plasticity rules across cortical development

Courtney E. Yaeger, Dimitra Vardalaki, Norma J. Brown, & Mark T. Harnett¹

¹McGovern Institute for Brain Research and Department of Brain and Cognitive Sciences, MIT, Cambridge, MA, USA

To whom correspondence should be addressed: Harnett (harnett@mit.edu)

Abstract

The modification of synaptic weights is critical for learning, while synaptic stability is required to maintain acquired knowledge. Single neurons have thousands of synapses within their dendritic arbors, and how the weights of specific inputs change across experience is poorly understood. Here we report that dendritic compartments receiving input from different presynaptic populations acquire distinct synaptic plasticity and integration rules across maturation. We find that apical oblique dendrites of layer 5 pyramidal neurons in adult mouse primary visual cortex receive direct monosynaptic projections from the dorsal lateral geniculate nucleus (dLGN), linearly integrate input, and lack synaptic potentiation. In contrast, basal dendrites, which do not receive dLGN input, exhibit NMDA receptor (NMDAR)-mediated supralinear integration and synaptic potentiation. Earlier in development, during thalamic input refinement, oblique and basal dendrites exhibited comparable NMDAR-dependent properties. Oblique dendrites gain mature properties with visual experience, and over the course of maturation, spines on oblique dendrites develop higher AMPA/NMDA ratios relative to basal dendrites. Our results demonstrate that cortical neurons possess dendrite-specific integration and plasticity rules that are set by the activity of their inputs. The linear, non-plastic nature of mature synapses on oblique dendrites may stabilize feedforward sensory processing while synaptic weights in other parts of the dendritic tree remain plastic, facilitating robust yet flexible cortical computation in adults.

Introduction

Adaptive behavior requires balancing the acquisition of new information with the retention of previously learned associations. Despite over half a century of work on synaptic plasticity, how neurons solve this tradeoff remains unknown. In adult visual cortex, primary sensory inputs are stable during normal visual experience^{1,2-7}, while cortical representations are readily remodeled⁸⁻¹¹. Dendrites of cortical neurons receive both primary sensory and intracortical inputs¹²⁻¹⁶ and play a key role in both synaptic plasticity and input compartmentalization. Convergent spatiotemporal input patterns arriving at a dendritic compartment can drive NMDAR-mediated calcium influx¹⁷ and trigger molecular cascades for synaptic modification¹⁸. Afferents from specific presynaptic populations can also target particular dendritic compartments^{16,19,20}, where plasticity rules can be location-dependent²¹⁻²⁷. However, it is unclear how distinct inputs utilize these mechanisms, and less is understood how input-specific synaptic weights are maintained across experience²⁸⁻³⁰. To investigate this stability-flexibility tradeoff for primary sensory cortical synapses, we first identified dLGN-recipient and non-recipient dendritic compartments in layer 5 pyramidal neurons (L5 PNs) in mouse primary visual cortex (V1). We compared synaptic integration and long-term potentiation of synapses at these two compartments in adults and across postnatal development.

Results

L5 PN oblique dendrites selectively receive thalamic input and exhibit distinct integrative properties from basal dendrites

Visual information from dLGN¹³ projects primarily to V1 layer 4 cells. In an analogous sensory cortex, first-order thalamic inputs also synapse on L5 PNs³¹, which integrate inputs from all cortical layers. Physiological data from juvenile V1¹⁴ and anatomical data³² suggest that dLGN inputs target the apical oblique dendrites of L5 PNs, which can reside in layer 4. To directly test where dLGN inputs make functional synapses on L5 PNs in mouse V1, we employed subcellular channelrhodopsin (ChR2)-assisted circuit mapping¹⁹. After viral expression of ChR2 in dLGN (Fig. 1a), we performed whole-cell patch-clamp recordings from V1 L5 PNs in acute slices from adult mice (P56+). Local photostimulation of ChR2-expressing dLGN boutons across the dendritic tree revealed monosynaptic connections restricted to apical oblique branches (Fig. 1b,c).

Given the specific targeting of dLGN inputs to L5 PN oblique dendrites, we asked whether these branches exhibited distinct properties compared to nearby basal dendrites (Fig. 1d). In acute slices from adult mice, basal dendrites displayed highly supralinear integration and

large local calcium influx in response to spatiotemporally-clustered two-photon glutamate uncaging (Fig. 1e,f,g), consistent with previous reports of NMDA spikes in juvenile cortex¹⁷. In contrast, oblique dendrites integrated inputs linearly until axosomatic action potential threshold was reached and did not show significant subthreshold calcium influx (Fig. 1e,f,g). These differences could not be explained by the size of uncaging events, the number of inputs, distance from the soma, action potential threshold, or $\delta V/\delta t$ prior to action potential (Supplemental Fig. 1). Thus, in adult V1 L5 PNs, oblique dendrites selectively receive dLGN input and exhibit a specialized linear integration mode.

Oblique dendrites lack synaptic potentiation in adult V1 L5 PNs

Because oblique dendrites did not exhibit large local calcium signals, we hypothesized that synapses on these branches should potentiate less than those on basal dendrites. Therefore, we tested synaptic potentiation within dendritic compartments by pairing focal electrical stimulation of presynaptic axons at basal or oblique dendrites with somatic current injection. A theta glass bipolar stimulating electrode was positioned within 10 μ m of either a basal or an oblique dendritic branch (Fig. 2a,b, Supplemental Fig. 2.) to generate a 1 to 2 mV excitatory postsynaptic potential (EPSP) in the presence of a GABA-A antagonist. EPSPs were paired with 20 ms somatic current injections that drove bursts of 2-4 action potentials. The peak of the EPSP and the peak of the first action potential were within 10 ms of each other, and 5 pairings at 10 Hz were repeated 30 times, with 10 seconds between epochs (Fig. 2c). This protocol strongly potentiated synapses on basal dendrites (Fig. 2d,f, Supplemental Fig. 2), similar to findings in juvenile cortex²¹. Potentiation at basal branches required pre- and postsynaptic coincidence and NMDARs (Supplemental Fig. 2). In contrast, synapses on oblique dendrites did not show any significant potentiation after pairing (Fig. 2e,f, Supplemental Fig. 2). Increasing the numbers of pairings did not change this outcome (Supplemental Fig. 2). These findings indicate that, unlike basal dendrites, oblique branches of L5 PNs in adult V1 lack Hebbian synaptic potentiation.

Synapses at oblique dendrites are plastic during a postnatal critical period

In V1, dLGN inputs are refined during early postnatal development^{33–35}, after which synaptic potentiation at some cortical synapses show a developmental decline^{36–38}. Therefore, we hypothesized that synapses on oblique L5 PN dendrites may exhibit NMDAR-mediated supralinear integration and plasticity during early postnatal development. Indeed, we found that at eye-opening (postnatal days 12-14), oblique and basal dendrites displayed similar NMDAR-

dependent supralinearities and large local calcium signals (Fig. 3a-c, Supplemental Fig. 3). These properties persisted into the canonical critical period (P18-22)^{39,40}. By 4 weeks of age (P28-P32), oblique dendrites had developed adult-like properties, with linear synaptic integration and small local calcium signals (Fig 3c, Supplemental Fig. 3). Synaptic plasticity at oblique dendrites followed the same developmental trajectory: except for P28, when integrative properties were adult-like, oblique and basal dendrites exhibited NMDAR-dependent synaptic potentiation at juvenile ages (Fig. 3d, Supplemental Fig. 3). These findings suggested that visual experience mediates the maturation of oblique dendrite properties; to test this, we conducted these same experiments in mice deprived of light from birth. In P28 dark-reared animals, oblique dendrites retained immature-like supralinear integration with large local calcium signals and synaptic potentiation (Fig. 3e, Supplemental Figs. 3). Dark-reared mice re-exposed to a normal light cycle did not develop adult-like integrative properties (Supplemental Fig. 3), indicating that the oblique compartment developed mature properties only during a specific window in development. Collectively, these results demonstrate a restricted developmental window in which visually-driven thalamic activity shifts the L5 PN oblique dendritic compartment towards a linear integration mode with synapses that do not potentiate.

Oblique dendrites develop distinct postsynaptic receptor composition

One possible interpretation of our data is that adult oblique dendrites lack large local calcium signals, integrate linearly, and do not potentiate due to a higher AMPA/NMDA ratio, as adult cortical AMPA receptors (AMPAARs) are significantly less Ca^{2+} -permeable than NMDARs^{41,42}. To test this, we compared AMPAR and NMDAR-mediated responses at single spines from basal and oblique dendrites at P21 and in adults. Glutamate uncaging produced AMPAR-mediated EPSPs within the physiological range at single spines, below the threshold for calcium influx (Fig. 4a, Supplemental Fig. 4). Then, Mg^{2+} -free ACSF containing the AMPAR antagonist DNQX was washed in and the uncaging protocol was repeated to assess synaptic NMDARs (Fig. 4b). The average maximum amplitudes of EPSPs under each condition were compared as an AMPA/NMDA ratio. At postnatal day 21, when oblique dendrites behave similarly to basal dendrites, spines from the two branch types had comparable AMPA/NMDA ratios. By adulthood, this ratio increased for oblique dendrites (Fig. 4c), indicating relatively less NMDAR-mediated synaptic conductance, consistent with linear integration, smaller local Ca^{2+} signals, and a decreased capacity for synaptic potentiation.

To provide complementary proteomic evidence for our observed changes in functional AMPA/NMDA, we acquired super-resolution images of oblique and basal dendrites and their

synaptic receptor content using epitope-preserving Magnified Analysis of the Proteome (eMAP, Fig. 4d)^{43,53}. Fixed slices from V1 of adult Thy1-GFP-M mice were expanded to 4x size and stained with antibodies against the presynaptic marker bassoon, the obligate NMDAR subunit GluN1, and GluA1 and GluA2, the predominant AMPAR subunits in cortex⁴⁴. Oblique and basal dendrites from L5 PNs were imaged with confocal microscope in ~18 µm-long segments (~75 µm expanded), and dendritic protrusions were annotated (Fig. 4e,f). Immature spines and protrusions without bassoon were excluded post hoc (although basal and oblique branches had similar numbers of immature and mature spines; Supplemental Fig. 4). For each spine head, the intensity of each fluorophore was spatially integrated (Fig. 4g), and the ratio of GluA1+GluA2/NR1 was taken. Oblique dendrite synapses exhibited higher AMPA/NMDA ratios than basal dendrites (Fig. 4h, Supplemental Fig. 4). This effect was pronounced in large spines (Fig. 4i). Taken together, these results indicate that oblique dendrites have relatively less NMDAR content and conductance, and this underlies the differences in integration and plasticity rules between basal and oblique dendritic compartments.

Discussion

Our results reveal that apical and basal dendritic compartments of adult V1 L5 PNs exhibit different integration modes and plasticity thresholds which are regulated by visual experience over the course of development. While basal dendrites consistently express NMDAR-dependent supralinear integration and synaptic potentiation, apical oblique dendrites show a developmentally-regulated transition away from NMDAR-mediated processes. Oblique dendrites of L5 PNs receive direct dLGN input, and during early visual experience, the synaptic AMPA/NMDA ratio on these branches increases, linearizing integration and limiting further synaptic potentiation by adulthood. Dark rearing disrupted this process, indicating a critical period for the maturation of synaptic properties in oblique dendrites. While critical periods have been previously described for cortical layers and inputs^{40,45}, our results are the first to show that critical periods also occur subcellularly, within dendritic compartments.

Our findings reveal that NMDAR-dependent synaptic potentiation is not universal at spiny synapses in adult cortex, an important discovery for both biological and artificial models of learning. The full dynamic range of plasticity in adult oblique dendrites is unclear: while our findings cannot rule out all possible plasticity mechanisms, limited NMDAR-mediated calcium influx constrains their potential to utilize conventional molecular cascades. Increasing AMPARs is likely one of many mechanisms involved in regulating developing synapses. Changes in excitatory receptor subtypes^{29,41,42,46–49}, kinase and phosphatase activity, as well as presynaptic

properties may also be contributing factors²⁸. Our results demonstrate a naturally-occurring example of plasticity regulation and establish a new tractable model for elucidating the mechanisms of synapse-specific stability, an important question for both experimental and computational neuroscience.

In contrast to what we observe in oblique dendrites, basal dendrites exhibit NMDAR-dependent supralinear integration and synaptic potentiation throughout maturation. Basal dendrites of L5 PN receive intracortical input^{16,20,22,50,51}, and effective cortical computation may require more flexibility and nonlinear processing of intracortical information than for feedforward thalamic input. Following developmental refinement, thalamocortical inputs become remarkably stable^{7,39,52}, while cortical representations remain plastic^{8–11}. Given that PNs in all layers of primary sensory cortex can receive both first-order thalamic and intracortical inputs^{12–15}, single neurons might utilize diverse plasticity thresholds within their dendrites to maintain synapse-specific plasticity without compromising representational fidelity. Subcellular input-specific plasticity regulation is a powerful new mechanism by which single cortical neurons can solve the tradeoff between flexibility and stability inherent to all learning systems.

Author Contributions

C.E.Y. and M.T.H. conceived of the experiments. C.E.Y. carried out all physiology experiments and analyses. D.V. conducted the eMAP experiments and C.E.Y. analyzed the data. N.J.B. performed viral injections and histology. M.T.H. supervised all aspects of the project and wrote the manuscript with C.E.Y.

Acknowledgements

We thank Mark Bear, Elly Nedivi, Josh Trachtenberg, and the Harnett laboratory for their comments and suggestions and Kwanghun Chung for generously sharing equipment. This work was funded by a Life Sciences Research Foundation postdoctoral fellowship (C.E.Y.), and a Vallee Foundation Scholars Award, the James W. and Patricia T. Poitras Fund, and the National Institutes of Health R01NS106031 (M.T.H.).

Competing interests

Authors declare that they have no competing interests.

Methods

Animals

All animal procedures were carried out in accordance with NIH and Massachusetts Institute of Technology Committee on Animal Care guidelines. C57BL6 male and female mice (Charles River Laboratories) were used in approximately equal numbers. Mice 8 weeks and older (P56+) were used for adult mouse experiments. For developmental timepoints, mice ages P10-P14, P18-22, and P28-P32 were used. All animals were kept in conventional social housing with unlimited food and water on a 12-hour light/dark cycle. For dark-rearing experiments, pregnant dams were moved to a dark room at E18 and pups were born and raised in complete darkness, with red light exposure during cage changes. Dark reared mice were ages P28-P32 at the time of experimentation. 8-week-old Thy-1-GFP-M mice (Jackson Laboratory) were used for eMAP experiments.

Slice preparation

Sucrose-containing artificial cerebrospinal fluid (sACSF) was used during the slicing procedure, containing (in mM): 90 sucrose, 60 sodium chloride, 26.5 sodium bicarbonate, 2.75 potassium chloride, 1.25 sodium phosphate, 9 glucose, 1.1 calcium chloride, and 4.1 magnesium chloride, with an osmolality of 295-302. The sucrose solution was partially frozen to create a small amount of slush and was kept ice-cold. Artificial cerebrospinal fluid (ACSF) was used for recovery and recording, containing (in mM): 122 sodium chloride, 25 sodium bicarbonate, 3 potassium chloride, 1.25 sodium phosphate, 12 glucose, 1.2 calcium chloride, 1.2 magnesium chloride, 1 ascorbate, and 3 sodium pyruvate, with an osmolality of 302-307. All solutions were saturated with carbogen, 5% CO₂ and 95% O₂. Acute slice preparation was consistent for all ages and experiments. Mice were put under isoflurane-induced anesthesia and decapitated. The brain was extracted in ice-cold sucrose solution in less than one minute. The brain was blocked at a moderate angle (approximately 20 degrees from coronal) to favor the preservation of apical dendrites in the occipital cortex. After the brain was mounted and submerged in ice-cold sACSF, a vibratome (Lieca VT1200S) was used to cut 300 μ m-thick slices, which were transferred to ACSF for 30-50 minutes at 36°C. Longer recovery times were used for tissue collected from younger animals. Following recovery, slices were kept at room temperature.

Patch-clamp recording

Recordings were performed in ACSF (concentrations noted above) at 34–36 °C. Intracellular recording solution contained (in mM): 134 potassium gluconate, 6 KCl, 10 HEPES, 4 NaCl, 4 Mg₂ATP, 3 NaGTP, and 14 phosphocreatine di(tris). Depending on the experiment, 0.05 mM Alexa 594, 0.1 mM Alexa 488, and/or 0.1 mM OGB-1 (Invitrogen) were added to the internal

solution. Whole-cell current-clamp recordings were obtained with a Dagan BVC-700A amplifier. Patch pipettes with thin-wall glass (1.5/1.0mm OD/ID, WPI) and resistances of 3-7 MΩ were used. Pipette capacitance was fully neutralized prior to break-in, and series resistance was kept fully balanced throughout, ranging from 5-30 MΩ. The liquid junction potential was not corrected. Current signals were digitized at 20kHz and filtered at 10kHz (Prairie View). L5 PNs were characterized by their large somas in layer 5, thick apical dendrites, broad arborization in layer 1, low input resistance, and prominent voltage sag.

Virus injection

For sCRACM experiments, AAV2-hSyn-hChr2(H134R)-mCherry (UNC Vector Core) was expressed in neurons in the dorsal lateral geniculate nucleus. Mice 6 weeks or older were injected 4 weeks or more before slice preparation. Under isoflurane anesthesia, mice were secured on a stereotaxic apparatus with a feedback-controlled heating pad (DC Temperature Control System, FHC). Slow-release buprenorphine (1 mg/kg) was administered subcutaneously. After scalp incision, a small burr hole was drilled over the injection site at the following coordinates relative to bregma: anterior-posterior 2.7-2.8 mm; medio-lateral 2.3-2.4 mm. A beveled microinjection pipette containing was lowered to a depth of 2.7-2.9 mm, and approximately 100 nL of virus was injected at a rate of 50 nL/min using a Nanoject. Following virus injection and a five minute rest, the pipette was removed and the incision was sutured. Accuracy of the injection was assessed in acute slices using two-photon microscopy. For image clarity, histology in Figure 1 was taken from a brain that was perfused, stored at 4°C overnight in 4% paraformaldehyde, transferred to PBS, and sectioned in 100 μm-thick slices. Sections were mounted, coverslipped, and imaged under a confocal microscope (Zeiss LSM 710 with a 10x objective, NA 0.45).

sCRACM

After 4 weeks or more of Chr2 expression in dLGN, acute slices of V1 were prepared. A two-photon laser scanning system (Bruker), with dual galvanometers and a MaiTai DeepSee laser, was used to confirm the presence of mCherry-expressing cell bodies in the dLGN. For all recordings, TTX (1 μM) and 4-AP (100 μM) were added to ACSF to isolate monosynaptic connections. Following whole-cell configuration, a 5 ms 473 nm full-field LED was used to determine if the neuron received inputs from axons containing Chr2. If the LED drove EPSPs or spikes, a 9 by 17 (400 x 800 μm) stimulation grid with 50 μm spacing was positioned over the area containing the entire neuron, aligned at the pia using two-photon imaging under low

magnification (4x, 0.16 NA air objective, Olympus) and Prairie View software. The stimulation grid controlled the location of a 473 nm laser beam (OptoEngine, LLC), and the duration of the light pulses was kept to 1-3 ms under <2 mW power. Each point on the grid was stimulated in order, progressing forward by column, with an interpoint delay of 1 s. 3-6 rounds of stimulation were averaged for each neuron. Baseline voltage was defined as the 50 ms before stimulation, and EPSP amplitudes were calculated as the baseline-subtracted maximum voltage within 50 ms after photostimulation. Population data was obtained by rotating the maps to align to the pia, overlaying the maps to align at the soma, normalizing peak voltages, and averaging across experiments.

Glutamate uncaging

Following whole-cell dialysis with a structural dye via the patch pipette, basal or apical oblique branches were localized using two-photon imaging. A pipette containing caged glutamate (4-methoxy-7-nitroindolyl-caged-L-glutamate or MNI-glutamate) diluted in ACSF (10 mM) was positioned just above the slice and over the recording site, and a picospritzer (Picospritzer III, Parker Hannifin) was used to puff a constant flow of caged glutamate into the region of interest. A second Mai-Tai DeepSee laser controlled by Prairie View software was used for photostimulation of MNI-glutamate at 720 nm. Uncaging was targeted just adjacent to spine heads. In the imaging pathway, a linescan was used for simultaneous calcium imaging. Laser intensity for both lasers was independently controlled (Conoptics). Linescan imaging was performed at 1300 Hz, with a dwell time of 8 μ s and a total scan time of less than 250 ms, with baseline fluorescence kept minimal and monitored throughout. Cells with signs of photodamage were excluded. The uncaging laser was calibrated to either a threshold calcium signal (~100% $\Delta F/F$) or an action potential, where the minimum power needed to drive either event was identified and used for all points. The uncaging dwell time was 0.2 ms, and the uncaging interval between multiple spines was 0.32 ms. Groups of 2-5 spines were stimulated independently and then in combination with other groups up to a total of 25-40 spines. Expected values were calculated by summing the average response of each group of spines. Ca^{2+} signals are expressed as $(F - F_{baseline})/F_{baseline}$. For acute blockade of NMDA receptors, the competitive antagonist D-AP5 (50 μ M) was used.

Spike-timing dependent plasticity

For local branch stimulation, theta glass (2.0/1.4mm OD/ID) housing a bipolar stimulating electrode (ISO-Flex, AMPI) was positioned within 10 μ m of a basal or apical oblique branch.

Stimulation intensity was calibrated to generate a small EPSP of 1-3 mV, typically requiring 5-20 μ A of current from the stimulating electrode. Ten minutes of baseline stimulation at 0.1 Hz was recorded to ensure stability of the EPSP. A -50 pA hyperpolarizing step was included to estimate input resistance. For plasticity induction, EPSPs were paired with a somatic current injection of 400-700 pA for 20 ms duration to produce a train of 2-4 action potentials. The peak of the first action potential was timed to be within 10 ms of the peak of the EPSP. Pairs were done in sets of 5 at 10 Hz, and sets of 5 were repeated 30 times at 0.1 Hz. After the induction period, EPSPs were monitored for at least 20 minutes. Inclusion criteria were as follows: resting membrane potential could fluctuate from baseline by no more than 3 mV, input resistance could not increase more than 20% of baseline; and series resistance had to be compensated fully throughout (<30 MOhms). Recordings were tested for baseline stability post-hoc using either correlation or linear regression (data not shown), and cells with significant changes in baseline recording were not included. The necessity of pre-post pairing was shown using the same recording set up but driving either the synaptic stimulation or the post-synaptic burst (and not both) during the induction period. For acute blockade of NMDARs, the competitive antagonist D-AP5 (50 μ M) was used. Throughout plasticity experiments, picrotoxin (100 μ M) was present in the bath to block GABAergic transmission in acute slices from adult mice and at P28. 10 μ M picrotoxin was used for acute slices at P21, and no picrotoxin was needed at P14.

Epitope-preserving Magnified Analysis of the Proteome

Mice were perfused with cold PBS followed by cold 4% PFA while under deep anesthesia (5% isoflurane). Brains were removed and kept in the same fixative overnight at 4°C and then washed with PBS at 4°C for at least 1 day. 1.0 mm coronal slices of primary visual cortex were cut on a vibratome and kept in PBS at 4°C until the day of processing. Slices were then incubated in eMAP hydrogel monomer solution⁵³ (30% acrylamide [A9099, MilliporeSigma, St. Louis, MO, USA], 10% sodium acrylate [408220, MilliporeSigma], 0.1% bis-acrylamide [161-0142, Bio-Rad Laboratories, Hercules, CA, USA], and 0.03% VA-044 (w/v) [Wako Chemicals, Richmond, VA, USA] in PBS), protected from light, at 4°C overnight. For gelation, slices were mounted between glass slides in eMAP solution and sealed in a 50 mL conical tube with nitrogen gas at positive pressure of 10-12 psi at 37°C for 3 hours. The excess gel around the slices was then removed. To reach a first expansion stage of 1.7x, the slices were incubated overnight in a solution of 0.02% sodium azide (w/v) in PBS at 37°C. Slices were trimmed to contain only parts of primary visual cortex and further sectioned with a vibratome to 75 μ m thickness (corresponding to ~40 μ m thickness of the pre-expanded tissue). Slices containing

good candidate cells – layer 5 pyramidal neurons whose apical trunk could be reconstructed at its full length in a single slice or at most two consecutive slices – were selected during live low-resolution confocal imaging sessions. These slices were trimmed to smallest possible samples of approximately 1.0 mm in both width and length. Slices were incubated in tissue clearing solution (6% SDS (w/v), 0.1 M phosphate buffer, 50 mM sodium sulfite, 0.02% sodium azide (w/v), pH 7.4) at 37°C for 6 hours, followed by incubation in preheated clearing solution at 95°C for 10 min. Cleared samples were thoroughly washed with PBS + 0.1% Triton X at 37 °C. Primary antibody staining was performed at 37°C overnight with the following antibodies: Anti-GFP (Life Technologies A10262), Anti-NMDAR1 (SYSY 114011), Anti-AMPA1 (SYSY 182003), Anti-AMPA2 (SYSY 182103), and Anti-Bassoon (SYSY 141004). For secondary staining, the following fluorescent antibodies were used: Bassoon: anti-Guinea pig-405 (AbCam ab175678); GFP: anti-Chicken-488 (Invitrogen A11039); NMDAR1: anti-Mouse-AF+555 (Invitrogen A32727); and AMPAR1 and AMPAR2: anti-Rabbit-AF+647 (Invitrogen A32733). Final expansion was performed just before imaging by putting the trimmed slices in 0.1 mM tris in distilled water, and approximately 4X total linear expansion was achieved. Slices were imaged using Leica TCS SP8 upright confocal DM6000 microscope equipped with a 63x HC PL APO CS2/1.2 W objective, hybrid detectors, and a white light laser. Within slices, intact L5b neurons were identified by their thick trunks and broad apical tufts. Within single neurons, both basal and oblique dendritic branches were imaged. To avoid photobleaching effects, no slice was imaged more than once, and basal and oblique dendrites were imaged in alternating order for each cell. Dendritic protrusions were analyzed using Fiji software. To draw regions of interest within spine heads in the GFP channel, a custom-written macro code was used to apply a median blur (2 pixels), threshold the image, and draw an ROI on the annotated protrusion. Using custom-written code in MATLAB, all color channels were thresholded to include only signals 2 S.D. above the mean fluorescence intensity, and signals from each channel were extracted from the ROI. The plane with peak antibody fluorescence was identified within the spine head ROI, and each channel's fluorescence signals within the plane were summed. Long, thin dendritic protrusions without enlarged heads were classified as filopodia (head diameter/neck diameter < 1.3) and excluded from the final analysis, as were spines with no detectable bassoon.

Data availability

All data and custom-written analysis code are available upon request.

References

1. Tan, L., Tring, E., Ringach, D. L., Zipursky, S. L. & Trachtenberg, J. T. Vision Changes the Cellular Composition of Binocular Circuitry during the Critical Period. *Neuron* **108**, 735–747.e6 (2020).
2. Wang, B.-S., Sarnaik, R. & Cang, J. Critical period plasticity matches binocular orientation preference in the visual cortex. *Neuron* **65**, 246–256 (2010).
3. LeVay, S., Wiesel, T. N. & Hubel, D. H. The development of ocular dominance columns in normal and visually deprived monkeys. *J. Comp. Neurol.* **191**, 1–51 (1980).
4. Wiesel, T. N. & Hubel, D. H. Effects of visual deprivation on morphology and physiology of cells in the cats lateral geniculate body. *J. Neurophysiol.* **26**, 978–993 (1963).
5. Wiesel, T. N. & Hubel, D. H. Single-cell responses in striate cortex of kittens deprived of vision in one eye. *J. Neurophysiol.* **26**, 1003–1017 (1963).
6. Clopath, C., Bonhoeffer, T., Hübener, M. & Rose, T. Variance and invariance of neuronal long-term representations. *Philos. Trans. R. Soc. Lond. B Biol. Sci.* **372**, (2017).
7. Rose, T., Jaepel, J., Hübener, M. & Bonhoeffer, T. Cell-specific restoration of stimulus preference after monocular deprivation in the visual cortex. *Science* **352**, 1319–1322 (2016).
8. Poort, J. *et al.* Learning Enhances Sensory and Multiple Non-sensory Representations in Primary Visual Cortex. *Neuron* **86**, 1478–1490 (2015).
9. Weskelblatt, J. B. & Niell, C. M. Distinct functional classes of excitatory neurons in mouse V1 are differentially modulated by learning and task engagement. *BioRxiv* (2019) doi:10.1101/533463.
10. Makino, H. & Komiyama, T. Learning enhances the relative impact of top-down processing in the visual cortex. *Nat. Neurosci.* **18**, 1116–1122 (2015).
11. Pakan, J. M. P., Currie, S. P., Fischer, L. & Rochefort, N. L. The impact of visual cues, reward, and motor feedback on the representation of behaviorally relevant spatial locations in primary visual cortex. *Cell Rep.* **24**, 2521–2528 (2018).
12. Harris, K. D. & Shepherd, G. M. G. The neocortical circuit: themes and variations. *Nat. Neurosci.* **18**, 170–181 (2015).
13. Antonini, A., Fagiolini, M. & Stryker, M. P. Anatomical correlates of functional plasticity in mouse visual cortex. *J. Neurosci.* **19**, 4388–4406 (1999).
14. Morgenstern, N. A., Bourg, J. & Petreanu, L. Multilaminar networks of cortical neurons integrate common inputs from sensory thalamus. *Nat. Neurosci.* **19**, 1034–1040 (2016).
15. Cruz-Martín, A. *et al.* A dedicated circuit links direction-selective retinal ganglion cells to the primary visual cortex. *Nature* **507**, 358–361 (2014).
16. Young, H., Belbut, B., Baeta, M. & Petreanu, L. Laminar-specific cortico-cortical loops in mouse visual cortex. *eLife* **10**, (2021).
17. Schiller, J., Major, G., Koester, H. J. & Schiller, Y. NMDA spikes in basal dendrites of cortical pyramidal neurons. *Nature* **404**, 285–289 (2000).
18. Malenka, R. C. & Bear, M. F. LTP and LTD: an embarrassment of riches. *Neuron* **44**, 5–21 (2004).
19. Petreanu, L., Mao, T., Sternson, S. M. & Svoboda, K. The subcellular organization of neocortical excitatory connections. *Nature* **457**, 1142–1145 (2009).
20. Gökçe, O., Bonhoeffer, T. & Scheuss, V. Clusters of synaptic inputs on dendrites of layer 5 pyramidal cells in mouse visual cortex. *eLife* **5**, (2016).
21. Gordon, U., Polsky, A. & Schiller, J. Plasticity compartments in basal dendrites of neocortical pyramidal neurons. *J. Neurosci.* **26**, 12717–12726 (2006).
22. Sjöström, P. J. & Häusser, M. A cooperative switch determines the sign of synaptic plasticity in distal dendrites of neocortical pyramidal neurons. *Neuron* **51**, 227–238 (2006).

23. Golding, N. L., Staff, N. P. & Spruston, N. Dendritic spikes as a mechanism for cooperative long-term potentiation. *Nature* **418**, 326–331 (2002).
24. Kumar, A., Barkai, E. & Schiller, J. Plasticity of olfactory bulb inputs mediated by dendritic NMDA-spikes in rodent piriform cortex. *eLife* **10**, (2021).
25. Weber, J. P. *et al.* Location-dependent synaptic plasticity rules by dendritic spine cooperativity. *Nat. Commun.* **7**, 11380 (2016).
26. Froemke, R. C., Poo, M.-M. & Dan, Y. Spike-timing-dependent synaptic plasticity depends on dendritic location. *Nature* **434**, 221–225 (2005).
27. Letzkus, J. J., Kampa, B. M. & Stuart, G. J. Learning rules for spike timing-dependent plasticity depend on dendritic synapse location. *J. Neurosci.* **26**, 10420–10429 (2006).
28. Abraham, W. C. Metaplasticity: tuning synapses and networks for plasticity. *Nat. Rev. Neurosci.* **9**, 387 (2008).
29. Turrigiano, G. G. The self-tuning neuron: synaptic scaling of excitatory synapses. *Cell* **135**, 422–435 (2008).
30. Meyer, D., Bonhoeffer, T. & Scheuss, V. Balance and stability of synaptic structures during synaptic plasticity. *Neuron* **82**, 430–443 (2014).
31. Constantinople, C. M. & Bruno, R. M. Deep cortical layers are activated directly by thalamus. *Science* **340**, 1591–1594 (2013).
32. Peters, A. & Feldman, M. L. The projection of the lateral geniculate nucleus to area 17 of the rat cerebral cortex. IV. Terminations upon spiny dendrites. *J. Neurocytol.* **6**, 669–689 (1977).
33. Gu, Y. & Cang, J. Binocular matching of thalamocortical and intracortical circuits in the mouse visual cortex. *eLife* **5**, (2016).
34. Sommeijer, J.-P. *et al.* Thalamic inhibition regulates critical-period plasticity in visual cortex and thalamus. *Nat. Neurosci.* **20**, 1715–1721 (2017).
35. Cang, J. *et al.* Development of precise maps in visual cortex requires patterned spontaneous activity in the retina. *Neuron* **48**, 797–809 (2005).
36. Kirkwood, A., Lee, H. K. & Bear, M. F. Co-regulation of long-term potentiation and experience-dependent synaptic plasticity in visual cortex by age and experience. *Nature* **375**, 328–331 (1995).
37. Jiang, B., Treviño, M. & Kirkwood, A. Sequential development of long-term potentiation and depression in different layers of the mouse visual cortex. *J. Neurosci.* **27**, 9648–9652 (2007).
38. Crair, M. C. & Malenka, R. C. A critical period for long-term potentiation at thalamocortical synapses. *Nature* **375**, 325–328 (1995).
39. Gordon, J. A. & Stryker, M. P. Experience-dependent plasticity of binocular responses in the primary visual cortex of the mouse. *J. Neurosci.* **16**, 3274–3286 (1996).
40. Feldman, D. E. Synaptic mechanisms for plasticity in neocortex. *Annu. Rev. Neurosci.* **32**, 33–55 (2009).
41. Kumar, S. S., Bacci, A., Kharazia, V. & Huguenard, J. R. A developmental switch of AMPA receptor subunits in neocortical pyramidal neurons. *J. Neurosci.* **22**, 3005–3015 (2002).
42. Hadzic, M., Jack, A. & Wahle, P. Ionotropic glutamate receptors: Which ones, when, and where in the mammalian neocortex. *J. Comp. Neurol.* **525**, 976–1033 (2017).
43. Ku, T. *et al.* Multiplexed and scalable super-resolution imaging of three-dimensional protein localization in size-adjustable tissues. *Nat. Biotechnol.* **34**, 973–981 (2016).
44. Cheng, D. *et al.* Relative and absolute quantification of postsynaptic density proteome isolated from rat forebrain and cerebellum. *Mol. Cell. Proteomics* **5**, 1158–1170 (2006).
45. Daw, N.W. Mechanisms of plasticity in the visual cortex. in *Visual Development* 207–233 (Kluwer Academic Publishers, 2006). doi:10.1007/0-387-30484-3_11.

46. Philpot, B. D., Cho, K. K. A. & Bear, M. F. Obligatory role of NR2A for metaplasticity in visual cortex. *Neuron* **53**, 495–502 (2007).
47. Erisir, A. & Harris, J. L. Decline of the critical period of visual plasticity is concurrent with the reduction of NR2B subunit of the synaptic NMDA receptor in layer 4. *J. Neurosci.* **23**, 5208–5218 (2003).
48. Liu, S. Q. & Cull-Candy, S. G. Synaptic activity at calcium-permeable AMPA receptors induces a switch in receptor subtype. *Nature* **405**, 454–458 (2000).
49. Clem, R. L., Celikel, T. & Barth, A. L. Ongoing in vivo experience triggers synaptic metaplasticity in the neocortex. *Science* **319**, 101–104 (2008).
50. Markram, H., Lübke, J., Frotscher, M., Roth, A. & Sakmann, B. Physiology and anatomy of synaptic connections between thick tufted pyramidal neurones in the developing rat neocortex. *J Physiol (Lond)* **500 (Pt 2)**, 409–440 (1997).
51. Thomson, A. M. & Bannister, A. P. Postsynaptic pyramidal target selection by descending layer III pyramidal axons: dual intracellular recordings and biocytin filling in slices of rat neocortex. *Neuroscience* **84**, 669–683 (1998).
52. Jaepel, J., Hübener, M., Bonhoeffer, T. & Rose, T. Lateral geniculate neurons projecting to primary visual cortex show ocular dominance plasticity in adult mice. *Nat. Neurosci.* **20**, 1708–1714 (2017).
53. Park, J., Khan, S., Yun, D.H., Ku, T., Villa, K.L., Lee, J.E., Zhang, Q., Park, J., Feng, G., Nedivi, E., et al. Epitope-preserving magnified analysis of proteome (eMAP). *Sci. Adv.* **7**, eabf6589. (2021).

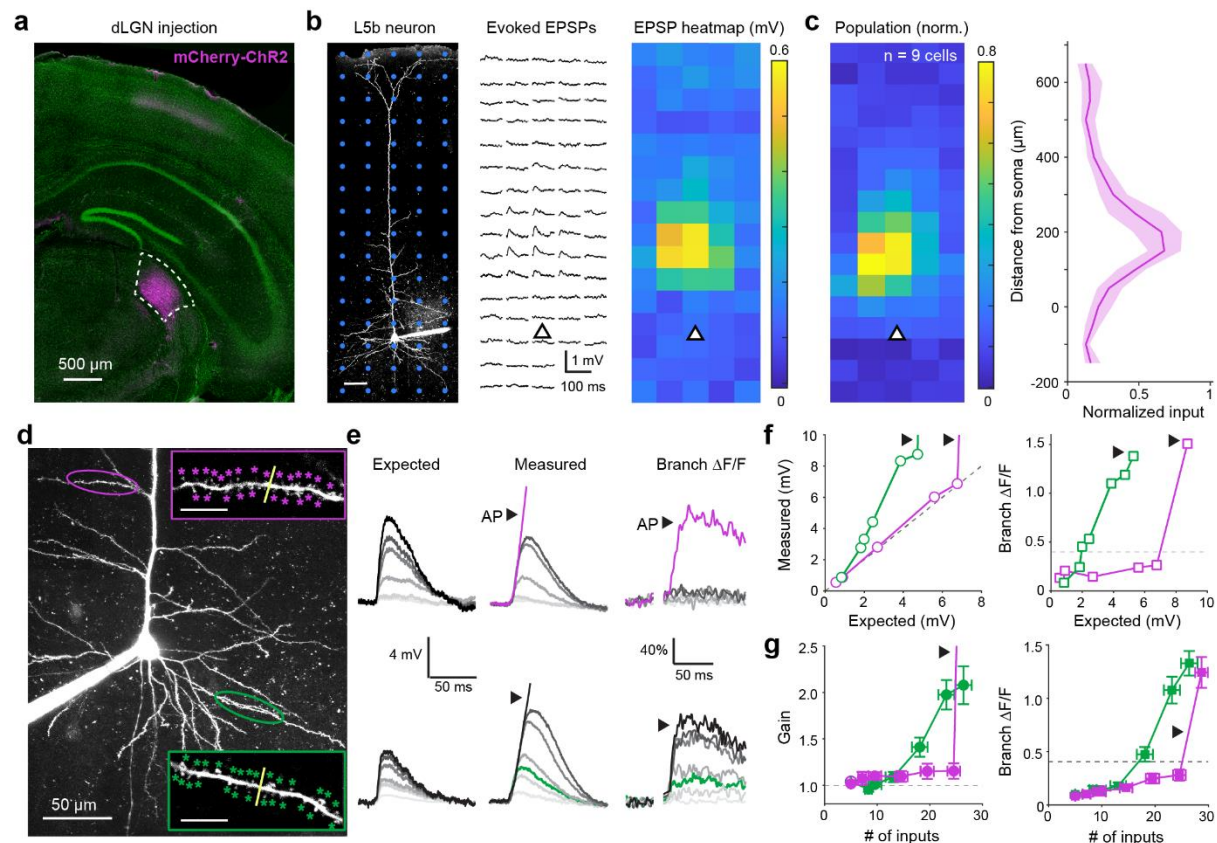


Figure 1: Apical oblique dendrites in V1 L5 PNs of adult mice are selectively targeted by dLGN inputs and exhibit distinct integrative properties compared to basal dendrites.

- Example confocal image of a coronal brain slice showing dLGN neurons infected with AAV2-hSyn-mCherry-ChR2.
- Left: Example two-photon image of a V1 L5 PN whole-cell recording with overlaid photostimulation grid (blue). Scale bar, 50 μm . Middle: Average evoked EPSPs from 6 repetitions of 473 nm photostimulation for the neuron and grid shown. Soma position is indicated by the triangle. Right: Heatmap of average evoked EPSPs. Each square is 50 μm .
- Left: Normalized heatmap of pooled L5 PNs ($n = 9$ neurons, 9 slices, 3 P56+ animals), aligned at the soma. Each square is 50 μm . Right: Mean normalized input as a function of depth for all neurons. Shaded region indicates the bootstrapped 95% confidence interval.
- Example two-photon z-stack of a L5 PN with glutamate uncaging sites indicated on an oblique (purple) and a basal (green) branch. Uncaging sites (stars) and linescan (yellow) are magnified in insets (scale bars: 10 μm).
- Expected EPSPs, measured EPSPs, and local branch Ca^{2+} signals for oblique (top) and basal (bottom) dendrites shown in d. Left: Expected voltages from linearly summed inputs. Middle: Measured EPSPs in response to increasing numbers of synchronous uncaging inputs. Stimulation of all inputs led to an action potential (AP, arrow). Right: Corresponding change in OGB-1 signal ($\Delta\text{F}/\text{F}$) with input summation.
- Measured voltage (left) and branch $\Delta\text{F}/\text{F}$ (right) as a function of expected voltage for the branches shown in d. Dashed line indicates linearity (left) and threshold Ca^{2+} signal (right).
- Adult population gain (measured/expected, left) and branch $\Delta\text{F}/\text{F}$ (right). $n = 13$ basal branches from 7 animals and 9 oblique branches from 6 animals. All animals were P56+. Basal AP removed for clarity. Basal vs oblique gain (AP excluded), Mann-Whitney U test: $p = 7.63\text{E}-04$; basal vs oblique $\Delta\text{F}/\text{F}$ (AP excluded), Mann-Whitney U test: $p = 1.08\text{E}-05$.

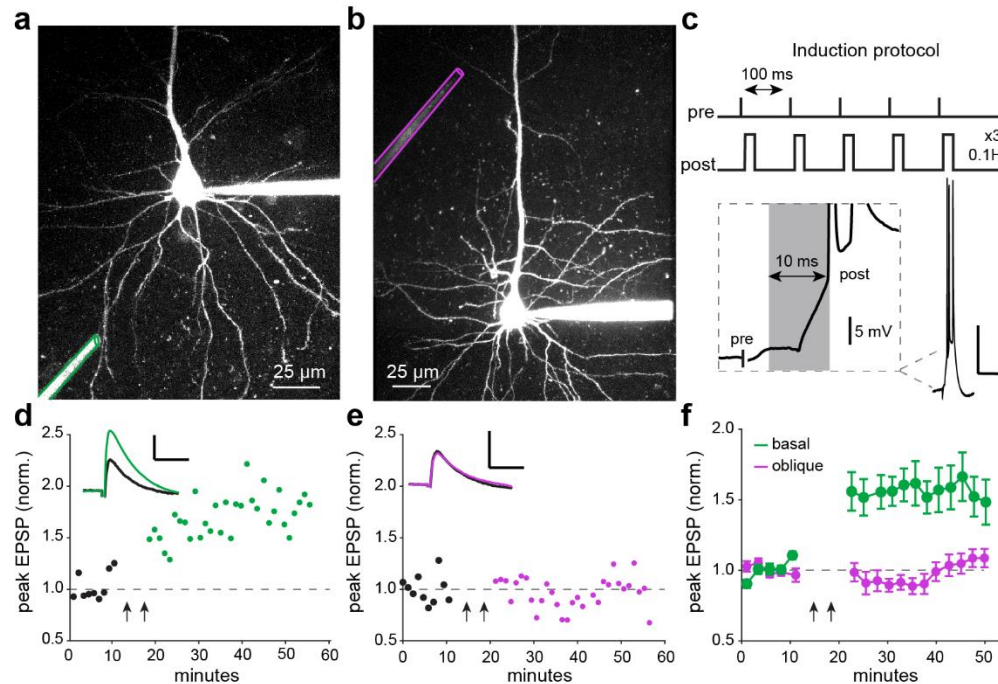


Figure 2: Oblique dendrites in V1 L5 PNs of adult mice lack long-term potentiation, unlike basal dendrites.

- Example two-photon z-stack of whole-cell recording with focal stimulation (green) near a basal dendrite.
- As in a, but for an oblique dendrite (purple).
- Plasticity induction protocol. 5 pairings of pre- and post-synaptic stimulation at 100 Hz, repeated 30 times at 0.1 Hz. Example trace below, right; inset shows the 10 ms interval between the peak of the evoked EPSP and the peak of the first action potential. Scale bar: 20 mV, 50 ms; inset: 5 mV, 5 ms.
- Example recording from the basal dendrite shown in a. After 10 minutes of baseline recording, the induction protocol is delivered (arrows denote start and stop). Inset shows average EPSP before (black) and after (color) pairing. Scale bar: 1 mV, 25 ms. Responses are 1 min binned averages.
- As in d, for the oblique dendrite shown in b.
- Mean normalized peak EPSP amplitude for neurons stimulated at basal (green) or oblique (purple) branches (2 min bins; $n = 10$ basal branches from 10 animals and 13 oblique branches from 12 animals. All animals were P56+). Error bars are s.e.m. Basal vs. oblique post-induction EPSP, Mann-Whitney U test: $p = 4.95E-63$.

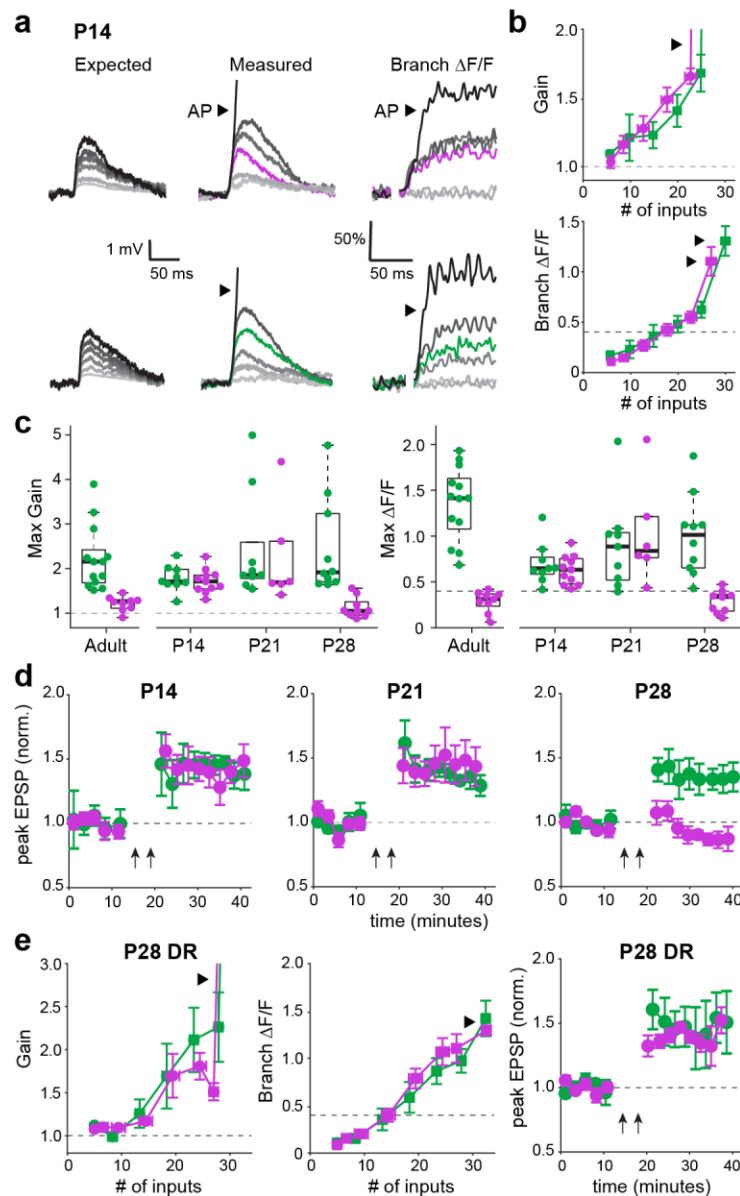


Figure 3: Developmental regulation of synaptic integration and plasticity in oblique versus basal dendrites.

- Expected (left), measured (middle), and $\Delta F/F$ (right) for oblique (top) and basal (bottom) dendrites from the same neuron from a P14 mouse. Note supralinear integration and large Ca^{2+} signals in both branches. Both are driven to action potential (AP, arrow).
- P14 population gain (measured/expected, left) and branch $\Delta F/F$ (right) ($n = 9$ basal branches and 9 oblique branches, both from 5 animals). Basal vs oblique gain*, $p = 0.33$; $\Delta F/F^*$, $p = 0.70$.
- Maximum gain (left) and local branch $\Delta F/F$ (prior to AP initiation, right) across developmental time points (Adult, P56+: n as in Fig. 1, basal vs oblique gain*, $p = 1.07\text{E-}04$; $\Delta F/F^*$, $p = 1.07\text{E-}04$. P14: n as in b, basal vs oblique gain*, $p = 0.54$; $\Delta F/F^*$, $p = 0.76$. P21: $n = 9$ basal branches, 4 animals, 6 oblique branches, 2 animals, basal vs oblique gain*, $p = 0.52$; $\Delta F/F^*$, $p = 0.68$. P28: $n = 10$ basal branches, 5 animals; 9 oblique branches, 5 animals, basal vs oblique gain*, $p = 2.17\text{E-}05$; $\Delta F/F^*$: $p = 4.33\text{E-}05$.

- d. Plasticity (as described in Fig. 2) in basal versus oblique dendrites at P14 (n = 5 basal branches from 5 animals and 5 oblique branches from 5 animals, basal vs oblique post-induction*, p = 0.79), P21 (n= 5 basal branches from 4 animals and 7 oblique branches from 6 animals, basal vs oblique post-induction*, p = 0.87), and P28 (n = 7 basal branches, 5 animals; 7 oblique branches, 4 animals, basal vs oblique post-induction*, p = 1.25E-13).
- e. P28 population gain (measured/expected, left) and branch $\Delta F/F$ (middle) in dark-reared (DR) mice (n = 9 basal branches and 10 oblique branches from 4 animals, basal vs oblique gain*, p = 0.78; $\Delta F/F^*$, p = 0.96). Plasticity for dark-reared animals (right) (n = 5 apical branches from 4 animals and 6 oblique branches from 6 animals, basal vs oblique post-induction*, p = 0.81).

*Mann-Whitney U test was used for all comparisons.

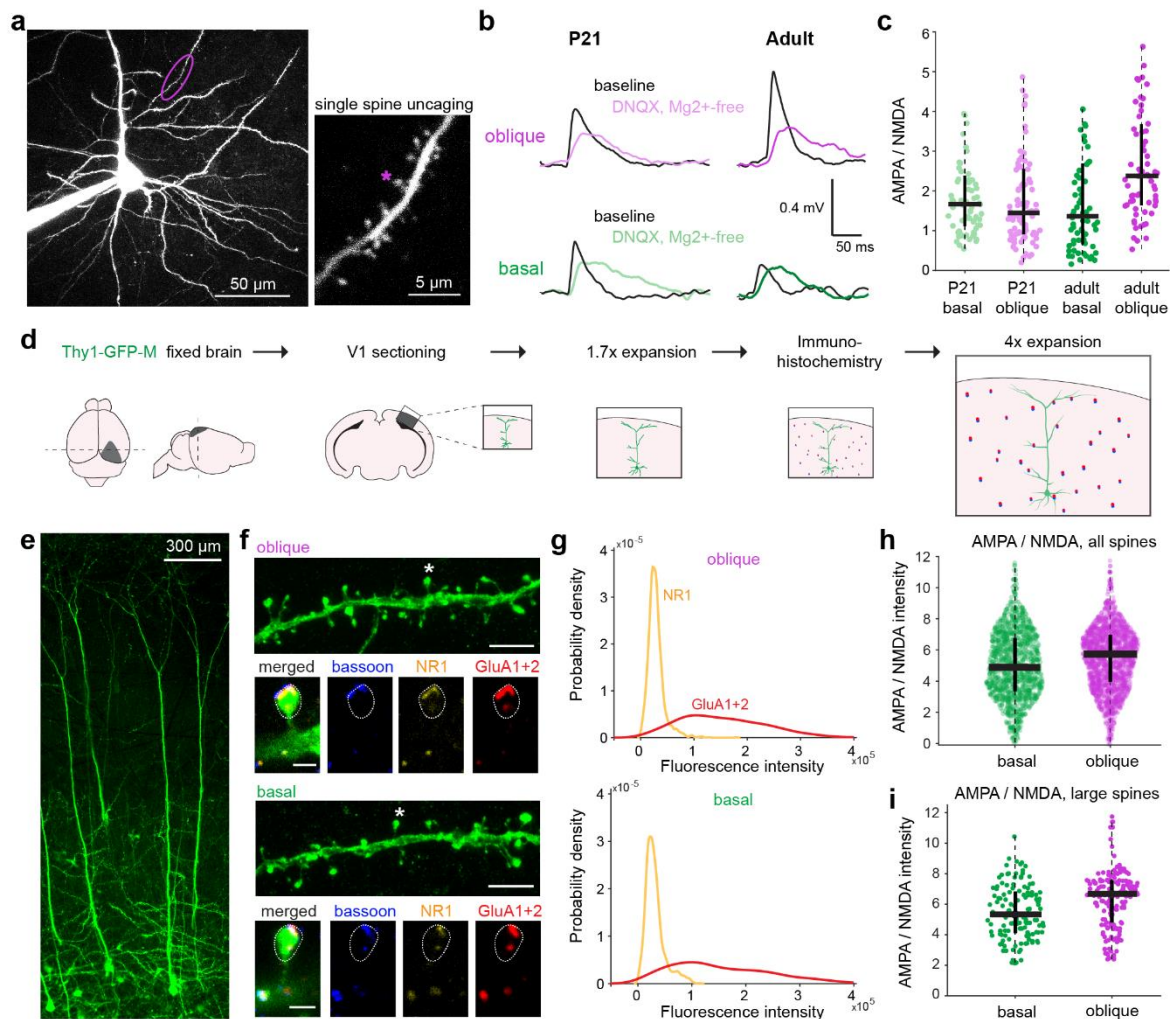
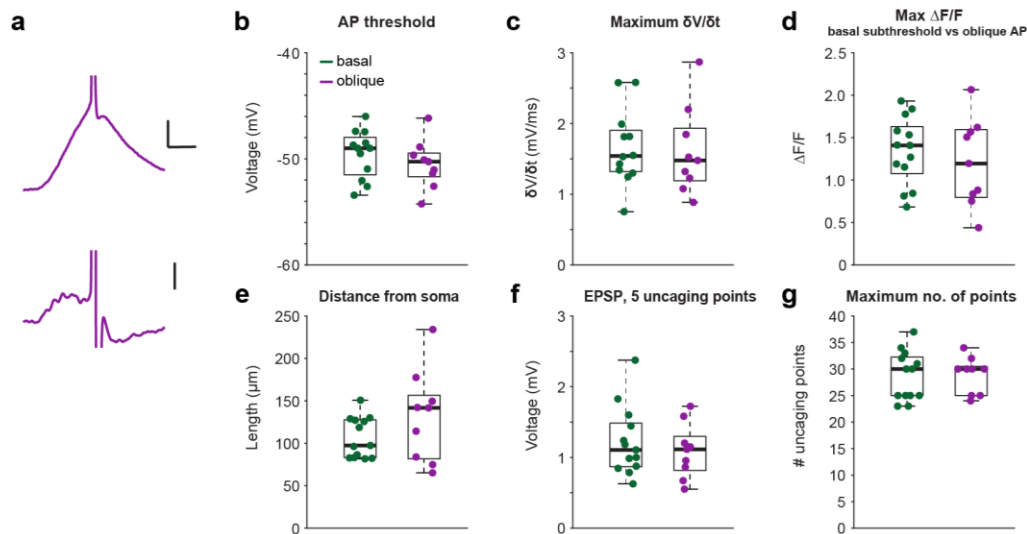


Figure 4: Changes in synaptic AMPA-to-NMDA ratio at oblique versus basal dendrites underlie differences in integration and plasticity.

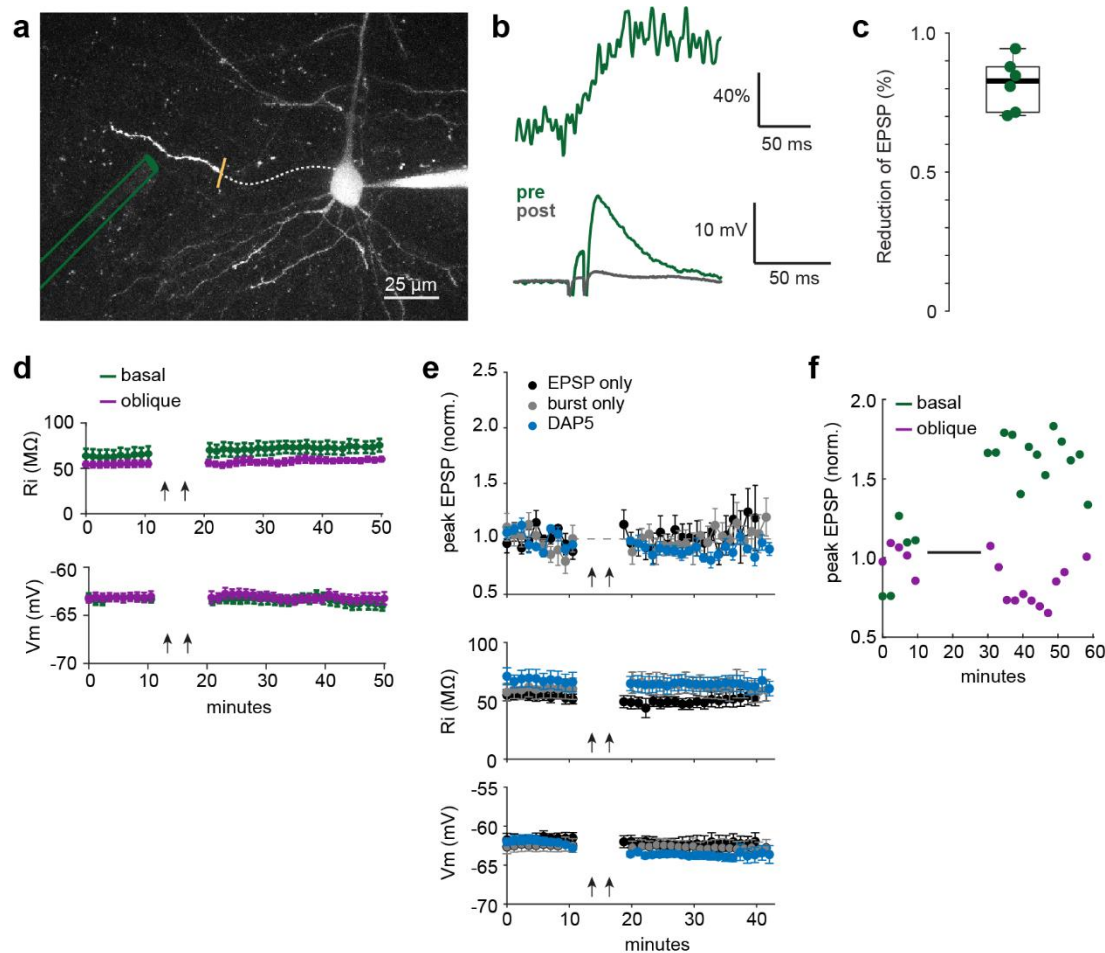
- Example two-photon image of a V1 L5 PN from a P21 mouse. An oblique dendrite (circled) is shown at higher magnification (right). Uncaging site indicated by star.
- Representative average EPSPs from uncaging at single spines in P21 (left) or adult (right) mice from oblique (top) and basal (bottom) dendrites. Black traces: control, colored traces: the same spine in DNQX+Mg²⁺-free ACSF.
- Functional single spine AMPA/NMDA ratios from basal and oblique dendrites in P21 and adult mice (P21: n = 72 basal spines from 4 mice and 89 oblique spines from 4 mice. Adult, P56+: n = 66 basal spines from 4 mice and 67 oblique spines from 5 mice). Outliers are not shown. P21 basal vs oblique, Mann-Whitney U test: p = 0.23; adult basal vs oblique, Mann-Whitney U test: p = 1.00E-04.
- Schematic of the Magnified Analysis of the Proteome (eMAP) experimental procedure.
- Confocal image of L5 PNs from a Thy1-GFP M P56+ mouse after 4x eMAP expansion.
- Example confocal images of expanded oblique (top) and basal (bottom) dendrites from the same neuron. For each branch, immunostaining for bassoon, NR1, and GluA1+2 is shown for one spine (indicated by star). Scale bar: 10 μ m, spine inset: 2 μ m.

- 581 g. Probability density of NR1 and GluA1+2 signals for all spines (n = 1,305 basal dendrite
- 582 spines and 1,719 oblique dendrite spines from 13 cells, 3 mice).
- 583 h. Ratio of AMPA/NMDA intensities for all spines: Mann-Whitney U test: $p = 8.30E-11$.
- 584 i. Ratio of AMPA/NMDA intensities for the largest 10% of basal and oblique spines (n = 131
- 585 basal dendrite spines and 171 oblique dendrite spines). Mann-Whitney U test: $p = 1.08E-04$.
- 586



Supplemental Figure 1. Properties of adult basal and oblique dendrites and experimental parameters of glutamate uncaging experiments.

- Example voltage waveform and corresponding $\delta V/\delta t$ for an AP evoked by glutamate uncaging at an oblique branch. Scale bar, top: 5 mV, 10 ms, bottom: 1 mV/s.
- Voltage thresholds for APs evoked by uncaging at basal (green) and oblique (purple) dendrites ($n = 12$ basal branches, 7 animals; 9 oblique branches, 6 animals. Mann-Whitney U test: $p = 0.27$).
- Maximum $\delta V/\delta t$ prior to AP initiation for uncaging at basal and oblique branches ($n = 12$ basal branches, 7 animals; 9 oblique branches, 6 animals. Mann-Whitney U test: $p = 0.64$).
- Maximum $\Delta F/F$ for subthreshold responses at basal dendrites and maximum $\Delta F/F$ in oblique dendrites following an AP ($n = 13$ basal branches, 7 animals; 8 oblique branches, 6 animals. Mann-Whitney U test: $p = 0.69$).
- Uncaging site distance from soma for basal and oblique dendrites ($n = 13$ basal branches, 7 animals, 9 oblique branches, 6 animals. Mann-Whitney U test: $p = 0.34$).
- EPSP amplitude for basal and oblique dendrites driven by 5 uncaging points ($n = 13$ basal branches, 7 animals; 9 oblique branches, 6 animals. Mann-Whitney U test: $p = 0.64$).
- Maximum number of uncaging points used in basal or oblique experiments ($n = 13$ basal branches, 7 animals; 9 oblique branches, 6 animals. Mann-Whitney U test: $p = 1$).

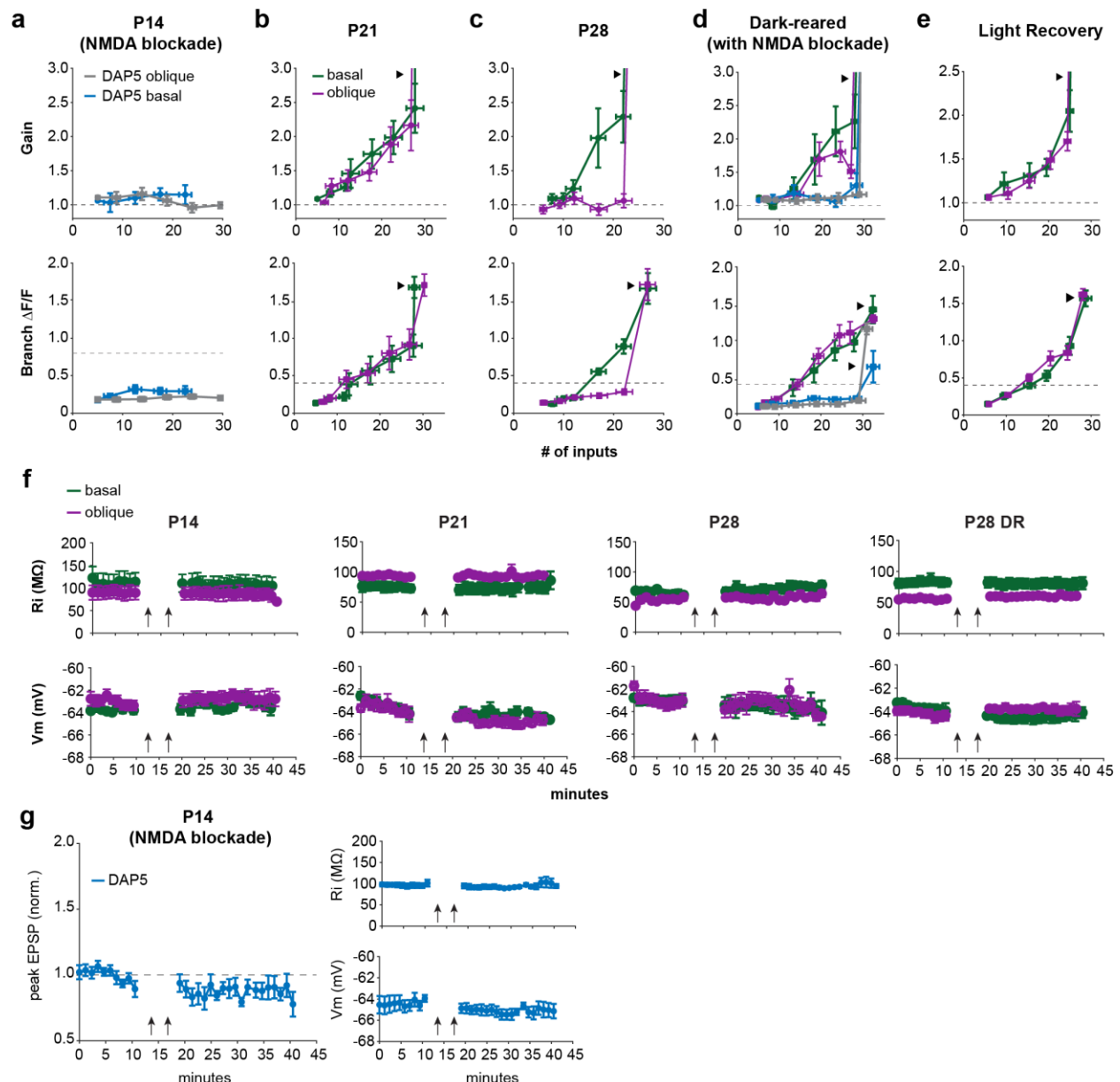


Supplemental Figure 2. Experimental measurement of local electrical stimulation spatial spread and properties of synaptic potentiation in adult L5 PN.

- Two-photon z-stack showing experimental set up. Theta glass pipette housing a bipolar electrode is positioned close to a basal branch to produce EPSPs and local Ca^{2+} signals. The branch is then severed with a laser (yellow) and EPSPs are measured again. The damaged proximal part of branch is indicated with a dotted line for clarity.
- A local branch Ca^{2+} signal (top) and somatically-recorded EPSP (bottom) were driven in the basal branch shown in a, prior to the laser cut (pre, green). Following severing of the branch, the EPSP is greatly reduced (post, gray).
- Percent reduction of peak EPSP amplitude following laser cutting, $n = 6$ basal branches from 6 neurons and 5 mice.
- Input resistance (top) and resting membrane potential (bottom) monitored throughout adult plasticity experiments shown in Figure 2. Neither corresponded with changes in synaptic potentiation.
- Coordinated pre- and post-synaptic activity and NMDA receptors are required for synaptic potentiation in basal dendrites. EPSPs (top) in basal dendrites following induction protocols with presynaptic-only stimulation (black, $n = 6$ cells, 5 animals), postsynaptic-only (gray, $n = 7$ cells, 4 animals), and pre/post pairing in the presence of D-AP5 (blue, $n = 5$ cells, 5 animals) with corresponding input resistance (middle) and resting membrane potential (bottom). Presynaptic-only or postsynaptic-only before versus after pairing comparisons were not statistically significant (pre-only, Mann-Whitney U test: $p = 0.42$, post-only, Mann-

Whitney U test: $p = 0.66$); pairing with D-AP5 showed small but statistically significant depression, Mann-Whitney U test: $p = 0.006$.

- f. EPSPs (2 min binned averages) from a basal and oblique dendrite before and after plasticity induction with 60 pairings. Despite double the number of pairings, the oblique branch does not potentiate.



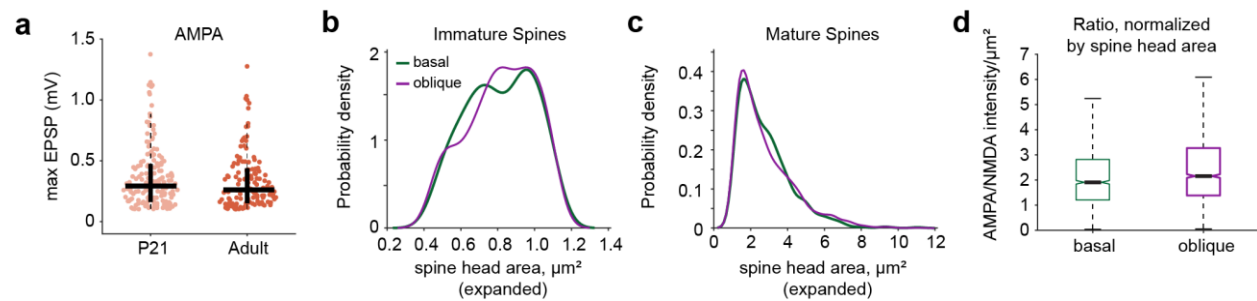
Supplemental Figure 3. Dendritic input-output relationships and plasticity properties for developmental timepoints and controls.

All panels are gain (top) and branch $\Delta F/F$ (bottom) vs. number of glutamate uncaging inputs.

- Blockade of NMDARs by D-AP5 eliminates supralinear gain and branch calcium influx for both basal (blue) and oblique (grey) dendrites in P14 mice.
- Basal and oblique dendrites exhibit supralinear gain and large Ca^{2+} signals in P21 mice under control conditions. Basal vs oblique gain*: $p = 0.29$; $\Delta F/F^*$: $p = 0.49$.
- In P28 mice, basal dendrites exhibit supralinear integration and large Ca^{2+} signals, in contrast to oblique dendrites, which are linear and lack Ca^{2+} signals prior to AP initiation. Basal vs oblique gain*: $p = 3.14\text{E-}06$; $\Delta F/F^*$: $p = 7.84\text{E-}04$. AP excluded in both comparisons.

- d. Both basal and oblique dendrites in P28 dark-reared animals integrate supralinearly with large Ca^{2+} signals. Basal vs oblique gain*: $p = 0.78$; $\Delta F/F^*$: $p = 0.96$, Mann-Whitney U test. These processes are NMDAR-dependent (D-AP5 blockade: basal, blue, oblique, grey).
- e. Both basal and oblique dendrites in dark-reared animals that are returned to normal light conditions for 2-4 weeks retain supralinear integration and large Ca^{2+} signals. Basal vs oblique gain*: $p = 0.75$; $\Delta F/F^*$: $p = 0.65$.
- f. Corresponding input resistance (top) and resting membrane potential (bottom) during plasticity experiments in Fig 3, for each developmental timepoint and dark-reared animals.
- g. D-AP5 prevents synaptic potentiation in P14 basal and oblique dendrites ($n = 4$ oblique dendrites in 3 animals, 2 basal dendrites in 2 animals, pre vs post induction*: $p = 1.41\text{E-}06$).

*Mann-Whitney U test was used for all comparisons.



Supplemental Figure 4. Amplitudes of uncaging-evoked single spine EPSPs and properties of spines in basal and oblique dendrites in expanded tissue.

- AMPA-mediated EPSP amplitudes for all spines used to measure functional AMPA/NMDA in P21 and adult mice (Mann-Whitney U test: $p = 0.43$).
- Probability density of immature spines in basal and oblique dendrites ($n = 392$ immature spines in basal dendrites, 513 immature spines in oblique dendrites, 13 cells, 3 animals, Mann-Whitney U test: $p = 0.34$).
- Probability density of mature spines in basal and oblique dendrites ($n = 1305$ spines in basal dendrites, 1719 spines in oblique dendrites, 13 cells, 3 animals, Mann-Whitney U test: $p = 0.77$).
- Ratio of AMPA/NMDA fluorescence intensity normalized by spine head area for spines in basal and oblique dendrites, Mann-Whitney U test: $p = 2.79\text{E-}08$.